

Article

Mineral Assemblages and Ore-Forming Physicochemical Conditions of the La'erma and Qiongmo Au–Se Deposits in the Western Qinling Orogen, Central China

Jiajun Liu ^{1,2,*}, Guoming Weng ^{1,2}, Emmanuel John M. Carranza ³, Degao Zhai ^{1,2}, Yinhong Wang ^{1,2}, Fangfang Zhang ^{1,2}, Shen Gao ^{1,2} and Lei Xu ⁴

- ¹ State Key Laboratory of Geological Processes and Mineral Resources, China University of Geosciences (Beijing), Beijing 100083, China; wengguoming@email.cugb.edu.cn (G.W.); dgzhai@cugb.edu.cn (D.Z.); wyh@cugb.edu.cn (Y.W.); zff@cugb.edu.cn (F.Z.); shen.gao@outlook.com (S.G.)
- ² School of Earth Sciences and Resources, China University of Geosciences (Beijing), Beijing 100083, China
- ³ Department of Geology, University of the Free State, Bloemfontein 9301, South Africa; ejmcarranza@gmail.com
- ⁴ Kunming General Survey of Natural Resources Center, China Geological Survey, Kunming 650100, China; xulei1992@mail.cgs.gov.cn
- * Correspondence: liujiajun@cugb.edu.cn; Tel.: +86-010-82321856

Abstract: The La'erma and Qiongmo Au–Se deposits are characterized by a paragenetic Au–Se association hosted in the siliceous formation of the Cambrian Taiyangding Group in the western Qinling Orogen, central China. The La'erma and Qiongmo Au–Se deposits, which are considered to be the Carlin gold deposits, comprise a variety of selenides, native gold, and stibnite coexisting with baryte. Four stages have been recognized: stage I comprises pyrite and quartz with minor stibnite; stage II is composed mainly of sulfides; stage III is composed mainly of selenides; and stage IV is dominated by quartz–baryte–dickite. Stages II and III are the main metallogenic stages. Based on changes in mineral assemblages, combined with fluid inclusions and thermodynamic data, we evaluated the physicochemical conditions of the main metallogenic stages. The $\log fS_2$ values of ore-forming fluids at stage II ranged between -10.44 and -14.60 with $\log fSe_2$ being less than -10.70 . Comparably, during stage III, which is characterized by numerous selenides, the $\log fS_2$ and $\log fSe_2$ ranged from -7.13 to -12.20 and -13.98 to -8.82 , respectively. The occurrence of baryte during the mineralization suggests a consistently oxidizing condition, which can effectively remove Au from fluids. More importantly, this study emphasizes that the oxidizing condition was only a fundamental prerequisite for the deposition of selenides, and a high $\Sigma Se/S$ ratio of the fluid ultimately controlled the precipitation of selenides. In the La'erma and Qiongmo deposits, intense water–rock reactions occurred as ore-forming fluids flowed into the Se-rich siliceous formations, resulting in an increase in the $\Sigma Se/S$ ratio of the fluid and in the precipitation of selenides.

Keywords: La'erma and Qiongmo deposits; Au–Se mineral associations; physicochemical conditions; high $\Sigma Se/S$; water–rock reactions



Citation: Liu, J.; Weng, G.; Carranza, E.J.M.; Zhai, D.; Wang, Y.; Zhang, F.; Gao, S.; Xu, L. Mineral Assemblages and Ore-Forming Physicochemical Conditions of the La'erma and Qiongmo Au–Se Deposits in the Western Qinling Orogen, Central China. *Minerals* **2024**, *14*, 507. <https://doi.org/10.3390/min14050507>

Academic Editor: Galina Palyanova

Received: 26 March 2024

Revised: 29 April 2024

Accepted: 30 April 2024

Published: 13 May 2024



Copyright: © 2024 by the authors. Licensee MDPI, Basel, Switzerland. This article is an open access article distributed under the terms and conditions of the Creative Commons Attribution (CC BY) license (<https://creativecommons.org/licenses/by/4.0/>).

1. Introduction

Selenium, a dispersed and strongly chalcophile element (e.g., Sb, Pb, Hg, and platinum-group elements, PGEs), is very rare, with an average abundance of 130 ppb in the upper crust [1]. Although it is more abundant than tellurium (2.7 ppb), which is another dispersed chalcophile element with an oxophilicity similar to Se, independent selenides are rarely found in deposits compared to tellurides [2–5]. The selenium in nature consists of independent selenides, isomorphism in Se-bearing sulfides, and adsorption. There are 155 Se-bearing minerals, including native selenium (Se) [6], selenides (Se combined with metal elements such as Cu, Pb, Bi, Pt, Pd, Au, Ni, Hg, Sb, Ag, Fe, etc.) [7], oxide (SeO₂) [8]

and oxysalts (such as $\text{CuSeO}_3 \cdot 2\text{H}_2\text{O}$ and PbSeO_3) [9]. Generally, independent selenides are uncommon in nature, and most selenium is hosted in sulfides and sulfosalts, such as pyrite, galena, sphalerite, stibnite, tetrahedrite, and metacinnabar [10–14], due to the similarity in crystal chemical properties between S and Se [10,15–17].

Currently, the number of independent Se deposits worldwide is rare. Representative examples of independent selenium deposits include the Pacajake and El Dragon deposits with Pb–Ba–Ag–Se element association in Bolivia [18,19] and the Yutangba deposit with Se–V–Mo in element association in Enshi, Hubei, China [20]. For Se-bearing deposits, the occurrence of Se can be divided into porphyry deposits, magmatic deposits, skarn deposits, volcanic-hosted deposits, hydrothermal deposits, and sedimentary-reworked deposits [21–23]. Almost all of the world's Se comes from porphyry Cu deposits.

The La'erma and Qiongmo Au–Se deposits, located in the southern subzone of the western Qinling Orogen, are typical Au–Se deposits. They are within the siliceous formation of the Cambrian Taiyangding Group. These deposits have attracted broad attention for the following reasons: coexistence of native gold with large amounts of independent selenides and the widespread occurrence of stibnite and baryte [15,24]. Since their discovery in 1985, extensively studies have been conducted on the geology, mineralogy, stable isotope geochemistry, fluid inclusions, and physicochemical conditions of the deposits. However, there has been scarce research conducted on the variation in physicochemical conditions in the metallogenic process and the factors of selenide precipitation. Through the analysis of mineral assemblages and physicochemical modeling, this contribution provides new insights into physicochemical conditions and the reasons for metallogenic processes. This study also enhances our understanding of the genesis of other selenide-bearing deposits.

2. Geological Setting

2.1. Regional Geology

As a major component of the Central China Orogenic Belt (CCOB), the WNW-striking Qinling Orogen in central China connects with the Qilian–Kunlun Orogen to the west and extends eastward to the Dabie–Sulu Ultra-High Pressure (UHP) zone (Figure 1a,b) [25,26]. The Qinling Orogen records a complex, multistage orogenic history associated with the collision of the North China Block (NCB), South Qinling Terrane (SQT), and South China Block (SCB) along the Shangdan and Mianlue sutures during Early Devonian and Middle/Late Triassic, respectively (Figure 1b) [25–27]. The SQT is composed of a thick pre-Sinian transitional basement, spanning from Sinian (uppermost of Neoproterozoic) to Devonian sedimentary sequences, which have been weakly deformed, with minor Carboniferous to Middle Triassic strata [28]. The formation of the Shangdan suture in the north has been interpreted to be related to the closure of the Shangdan Ocean in the Early Devonian, which is a branch of the proto-Tethys Ocean that underwent northward subduction toward the North Qinling Terrane (NQT) during the Early Palaeozoic [26,27,29]. The Mianlue suture records evidence of the northward subduction of the Mianlue Ocean from Permian to Early Triassic, and the collision between the SCB and SQT along the Mianlue Suture during the Middle–Late Triassic [10,28,30]. The collisional collapse and compressional deformation occurred during the Early Jurassic to Middle Jurassic and Late Jurassic to Early Cretaceous, respectively, representing the intracontinental tectonic process [25,31].

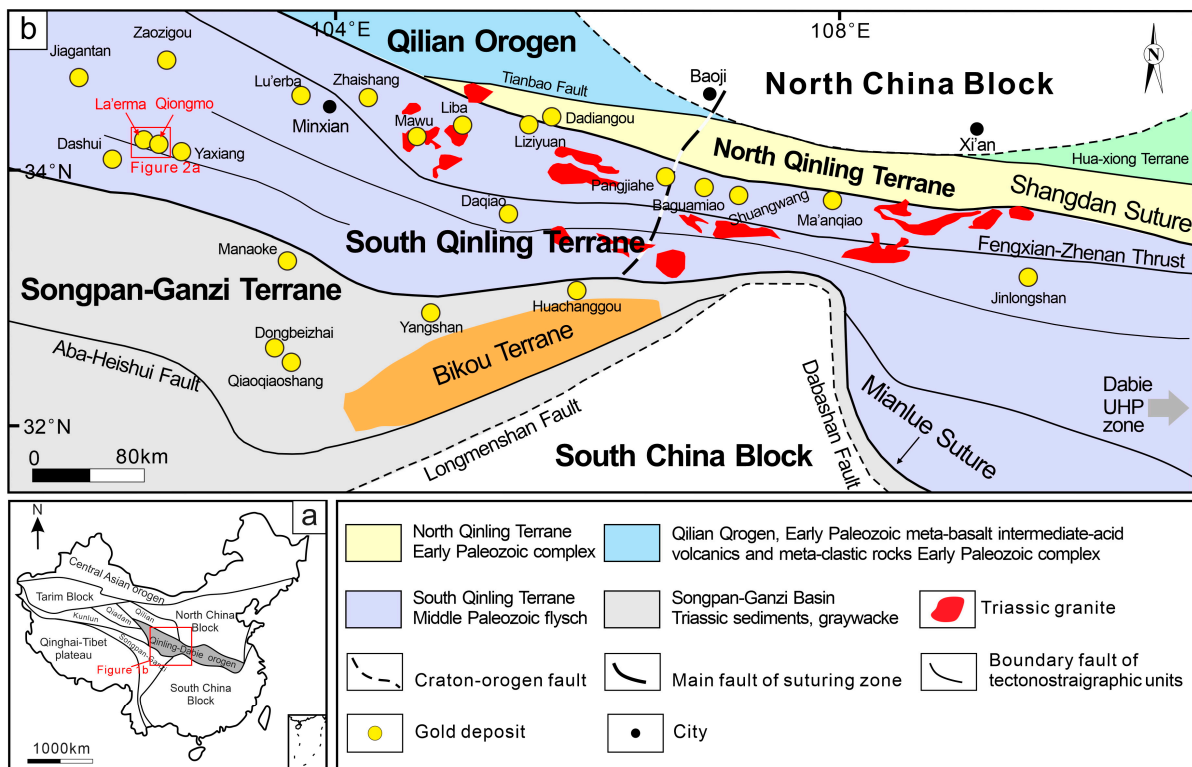


Figure 1. (a) Major tectonic division of China and **(b)** geological map of the Qinling Orogen, showing the distribution of the most important gold deposits and granitic intrusions (modified from Liu et al. [30]).

The Qinling Orogen is commonly subdivided into the western Qinling Orogen and the eastern Qinling Orogen along the Baocheng railway (Chengxian–Huixian–Fengxian fault; Figure 1b). Stratigraphically, the western Qinling Orogen includes Early Palaeozoic to Triassic marine sedimentary rocks characterized by the presence of greenschist facies, and unmetamorphosed Triassic turbidites [28,32]. In the western Qinling Orogen, there are widespread Triassic granitoids, which resulted from the subduction of the Mianlue oceanic plate and the amalgamation between SCB and NCB [33], consisting of granite, monzogranite, and diorite granite that host abundant mafic microgranular enclaves, minor lamprophyre, and minette or carbonatite dikes. The granitoids are metaluminous to peraluminous, moderate to high-K calc-alkaline, and display enrichment in LILE and LREE but depletion in HFSE [28]. The older granitoids formed during the 250–235 Ma period and are distributed in the northern part of the western Qinling Orogen, whereas younger magmatism (225–210 Ma) is located in the of central and eastern parts of the western Qinling Orogen [10]. The former exists in arc magmas related to subduction, whereas the latter is thought to have formed in a syn-collision-to-post-collision setting.

2.2. Deposit Geology

The Cambrian stratabound gold deposits, including the La'erma deposit, Qiongmo deposit, and the Yaxiang gold ore occurrence, are located in the southern subzone of the western Qinling Orogen (Figure 2a) [34,35].

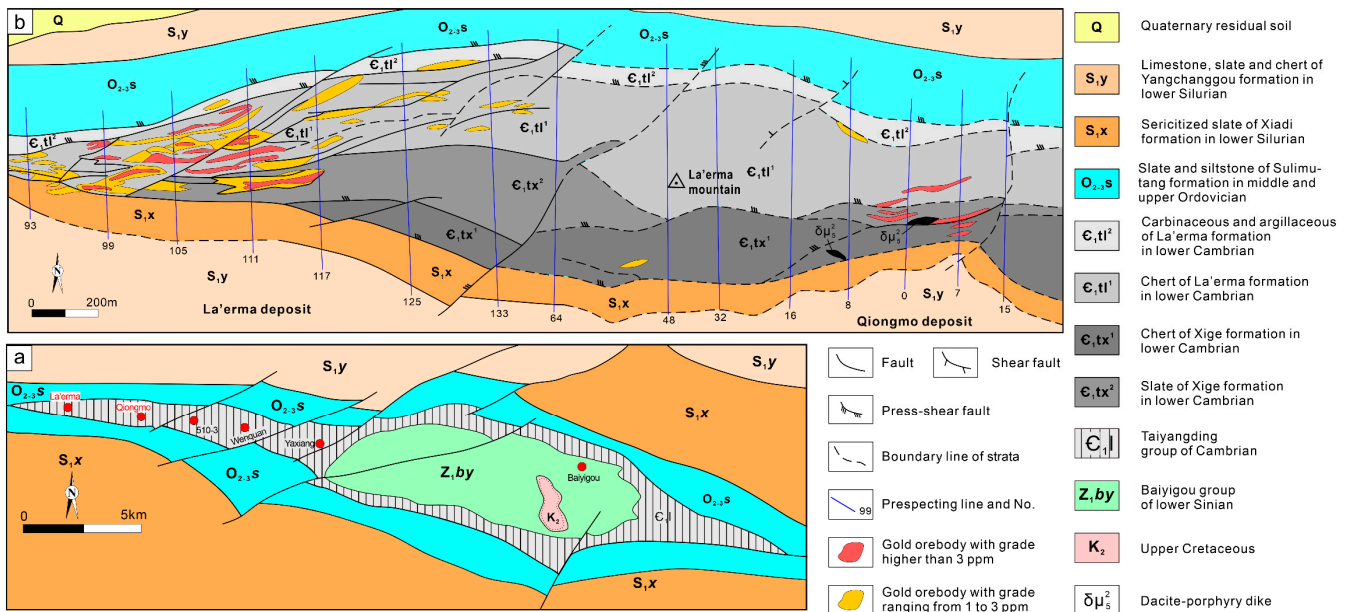


Figure 2. (a) Geological sketch map of the Cambrian Stratabound gold deposits in the southern subzone of the western Qinling Orogen (modified from Liu et al. [34]); (b) geological map of the La'erma and Qiongmo Au–Se deposits (modified from Mao et al. [15]).

2.2.1. Stratigraphy

In this area, the Baiyigou Group of lower Sinian age, Taiyangding Group of Cambrian age, Sulimutang Formation of middle-upper Ordovician age, Xiadi Formation of lower Silurian age, and Yangchanggou Formation of lower Silurian age are exposed sequentially from the core to the rim of the anticline (Figure 2a). Gold mineralization at the La'erma and Qiongmo Au–Se deposits are hosted by the siliceous formation of the Cambrian Taiyangding Group, which consists of the Yaxiang, Xige, and La'erma Formations, which have distinct stratigraphic, lithologic, and structural characteristics (Figure 2) [36]. The up to 1000 m-thick siliceous formation, which was formed by submarine exhalative sedimentation, consists mainly of a series of carbonaceous cherts and slates with minor carbonate lens [34,37]. The siliceous formation is characterized by the enrichment of organic carbon. There are no significant igneous rocks outcrops, but there are some quartz diorite, granodiorite, and dacite porphyry dikes, which are several hundred meters in length, and 1 to 2 m-thick, that intruded the Lower Cambrian strata along faults (Figure 2b) [38,39].

2.2.2. Structural Geology

The La'erma and Qiongmo Au–Se deposits are located in the western segment of the axial surface of the westerly plunging Bailongjiang anticline (Figure 2b). They are situated in a group of north-dipping shear zone that is bounded by two dextral strike-slip faults [40]. The shear zone, comprising a number of nearly parallel strike-reverse faults, spans 1950 m in length and 200–400 m in width with E–W-strike and dip directions of 15°–20° and a dip angles of 70°–85° [41]. At the mine scale, gold orebodies have been discovered in the E–W-striking faults, which are characterized by brittle fractures and siliceous brecciation that played an important role in the source of ore-forming materials, the migration of ore-forming fluids, and mineral precipitation. The orebody cluster is bounded by faults F2 and F7 (Figure 2b). The EW-striking faults are cut by the secondary NE- and N–S-striking faults.

2.2.3. Orebody Geology

The La'erma and Qiongmo Au–Se deposits consist of over 100 ore bodies, most of which are located in the La'erma deposit to the west. The discovered orebodies are stratabound and lenticular in shape, and are distributed along faults and fracture zones

that are E–W-trending and mostly NW-dipping with dip angles of 60°–80° (Figure 3). The orebodies also follow the bedding planes, lithological contacts and anticlinal fold hinges [15,38]. The west-central part of the La’erma deposit (lines 91–121) is the main mineralized section, which is approximately 1250 m long and 200–320 m wide. The lengths of the orebodies in the La’erma deposit range from 40 m to 450 m and are 1.0–38.05 m in width with vertical extents of 80–200 m [41]. The Au grade of these orebodies ranges from 1.00 to 25.00 g/t with the highest grade being 66 g/t. Orebodies in Qiongmo deposit are 60–330 m in length, with a thickness of 1.0–8.49 m with vertical extents of 40–430 m, carrying 1.0–6.14 g/t Au. The orebodies are large and the mineralization is concentrated where the fracture converges to the west, and they are small where the fractures spread out to the east.

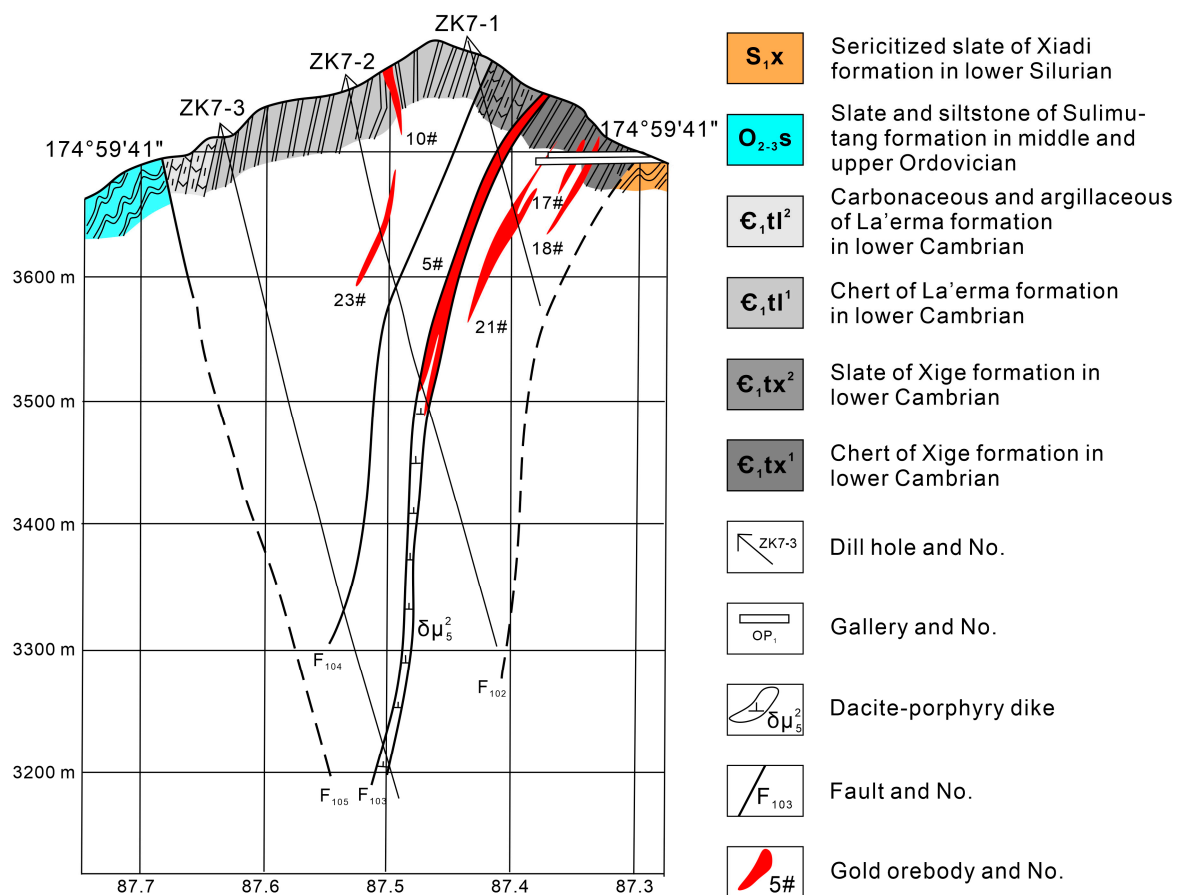


Figure 3. Geological cross section of line 7 in the Qiongmo Au–Se deposit (modified from Liu et al. [15]).

Three types of ores have been identified based on their host rocks: chert type, slate type, and dacite porphyry type (Figure 4) [15,35]. The chert type, which can be divided into layered chert ore and silicified ore, is the best mineralized ore, containing 75%–80% of the total ore with gold grades between 1.0 and 7.0 g/t [15]. However, the slate type represents the most exposed orebodies with relatively low gold grades of 2.0–5.0 g/t. The dacite-porphyry-type ores, mostly occurring in the Qiongmo deposit, exhibit a high degree of variability in gold grade. In addition, locally enriched Cu, U, Mo, Sb, V, and Zn, and particularly Se, In, and PGE, can sometimes be of economic interest [34–37]. The strata show a high Se content, with chert-type ores having the highest Se content at 33.9 ppm and slate type at 18 ppm. In addition, porphyry’s Se content varies from 14.1 to 57.5 ppm [35].

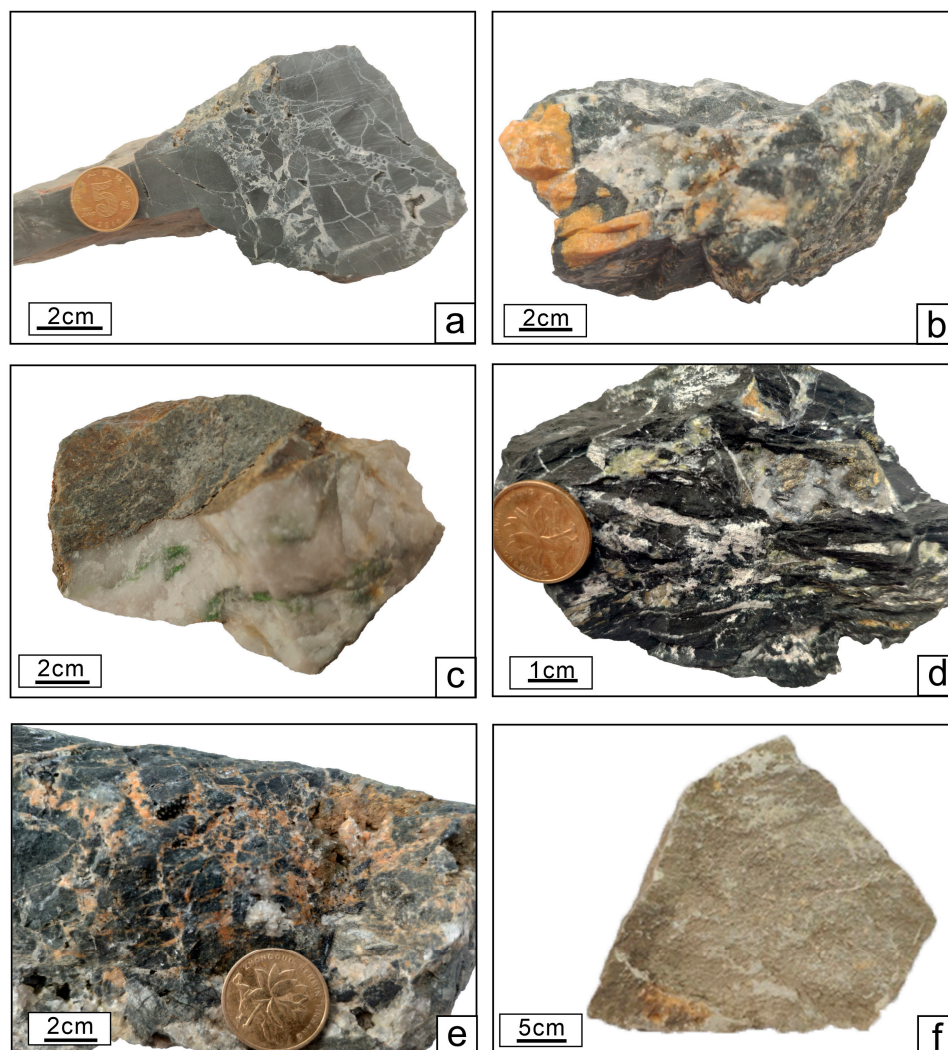


Figure 4. Representative photographs in hand specimens. (a) Brecciated chert-type ore; (b) chert-type ore; (c) chert-type ore; (d) brecciated slate-type ore; (e) brecciated silicified slate-type ore; (f) dacite porphyry-type ore.

The mineral assemblages and ore-forming elements of the La’erma and Qiongmo Au–Se deposits are complex. More than 80 minerals have been discovered, including the following: sulfides of Cu, Pb, Zn, As, Mo, Ni, and Sb; selenides; U-bearing minerals; and a large amount of oxides [36]. The main sulfides include pyrite, marcasite, and stibnite. And the main selenide is tiemannite (Figure 5). More importantly, the La’erma and Qiongmo Au–Se deposits are characterized by large amounts of baryte coexisting with native gold, selenides, and sulfides (Figure 5).

The La’erma and Qiongmo Au–Se deposits exhibit a sequence of brecciated, stockwork, veined, and disseminated structures, replacing each other from the mineralization center towards the outer areas. The ores exhibit the framboidal, euhedral–subhedral granular, anhedral granular, zonal, mosaic, metasomatic relict, graphic, porphyroclastic, and stress textures. Hydrothermal alteration at La’erma and Qiongmo are widespread and includes silicification, pyritization, baritization and dickitization. Silicification, the most pervasive alteration, is the most closely related to gold mineralization.

Previous studies have detailed the mineral paragenesis of the La’erma and Qiongmo Au–Se deposits, identifying four metallogenic stages (Figures 5 and 6) [15,38,42]. Stage I comprises pyrite and quartz with minor stibnite. Stage II is represented by the association of pyrite–marcasite–quartz–native gold. In stage II, the native gold commonly coexists with

stibnite. There are a large of sulfides, including chalcopyrite, marcasite, bornite, pyrrhotite, polydymite, sphalerite, and galena. Stage III mainly includes stibnite–selenides–native gold–quartz–baryte. This stage is important as it involves the formation of selenides, such as tiemannite, clausthalite, antimonselite, kullerudite, and an unnamed $\text{Ni}_3\text{As}_3\text{S}_3\text{Se}$ mineral phase [43,44]. In this stage, the native gold occurring in droplets or anhedral coexists with stibnite and tiemannite (Figure 5). Selenides, such as tiemannite, antimonselite, clausthalite, and kullerudite, often coexist with sulfides like stibnite and famatinite in baryte and quartz. In the late stage III, subhedral–anhedral cinnabar, realgar, and orpiment occur in a baryte–quartz vein. Stage IV is dominated by quartz–baryte–dickite. Stages II and III are the main metallogenic stages.

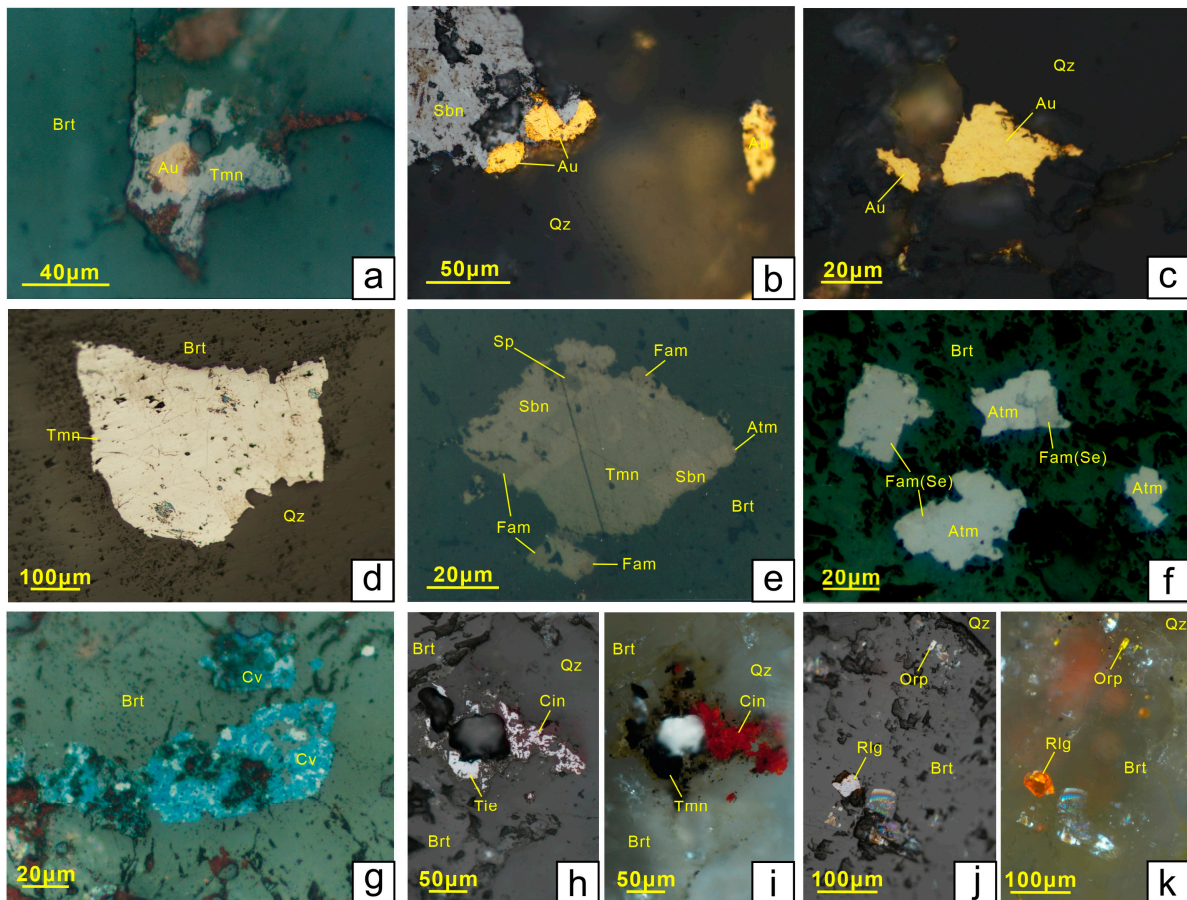


Figure 5. Representative micrographs of mineral assemblages from the La'erma and Qiongmo Au–Se deposits. (a–c) Native gold intergrowing with tiemannite, stibnite, baryte, and quartz; (d) tiemannite intergrowing with baryte [45]; (d,e) tiemannite coexisting with antimonselite, famatinite, sphalerite, and stibnite [46]; (f) antimonselite coexisting with selenium famatinite and baryte; (g) covellite coexisting with baryte; (h,i) tiemannite coexisting with cinnabar, baryte, and quartz; (j,k) mineral assemblages of orpiment and realgar occur in the baryte. Abbreviations: Au = native gold; Tmn = tiemannite; Sbn = stibnite; Atm = antimonselite; Fam = famatinite; Sp = sphalerite; Fam (Se) = selenium famatinite; Cv = covellite; Cin = cinnabar; Orp = orpiment; Rlg = realgar; Brt = baryte; Qz = quartz.

Minerals	Stage I	Stage II	Stage III	Stage IV
Pyrite	██████	██████	————	
Stibnite	————	————	██████	————
Chalcopyrite		██████	————	
Marcasite		██████		
Bornite		██████		
Pyrrhotite		██████		
Polydymite		————		
Sphalerite		————	██████	
Galena		————	————	
Native gold		————	██████	
Famatinite			██████	
Tetrahedite			██████	
Vaesite			————	
Covellite			————	
Tiemannite			██████	
Clausthalite			————	
Antimonelite			————	
Kullerudite			————	
Permingeatite			————	
Ferroselite			————	
Cinnabar			—	—
Realgar			—	————
Orpiment			—	————
Quartz	██████	██████	██████	██████
Baryte		————	██████	██████
Dickite			—	██████

Figure 6. Paragenetic sequence of minerals in the La'erma and Qiongmo Au–Se deposits.

3. Sample and Analytical Methods

In this study, all mineral samples originate from the La'erma and Qiongmo Au–Se deposits. Firstly, thin polished sections of samples were examined under the reflected light using a Leica DM 2700P polarizing microscope at Institute of Geochemistry Chinese Academy of Sciences (IGCAS), Guiyang, China. Then, the electron-microprobe work was conducted at the State Key Laboratory of Ore Deposit Geochemistry (SKLOGD), Institute of Geochemistry, Chinese Academy of Sciences, Guiyang, China. Electron Probe Laboratory of Institute of Geochemistry Chinese Academy of Sciences used a JEOL JXA-733, equipped with wave and energy dispersive and back-scattered detectors. The major and minor elements compositions of sulfides, selenides, and native gold were measured, and the BSE images were obtained. The conditions for electron-microprobe work were carried out at accelerating voltage of 15 kV, current of 20 nA, and 1 diameter, and 20 s counting time. The standards (and corresponding) radiations used included Ag (Ag L α), Au (Au M α), As (As L α), Cu (Cu K α), Fe (Fe K α), Hg (Hg M α), Co (Co K α), Ni (Ni K α), Sn (Sn K α), Pb (Pb M α), S (S K α), Sb (Sb L α), Se (Se L α), Te (Te L α), Zn (Zn L α). Application of ZAF correction in quantitative analysis processing.

4. Results

4.1. Native Gold

The La'erma and Qiongmo Au–Se deposits contain Au-bearing minerals, including invisible Au and microscopic native gold. Pyrite and marcasite are the main mineral that host invisible Au. Native gold, which is the predominant form of gold present, is produced in various forms, including encapsulated gold, intergranular gold, fissure gold, and a small amount of associated gold (Figure 5a–c). Of these, encapsulated gold is the most common, with native gold encapsulated in stibnite, baryte, quartz, tiemannite, and

dickite. Intergranular gold is distributed between the coexisting quartz, baryte, dickite, and stibnite grains. Fissure gold is distributed along fractures in quartz–baryte veins and altered host rocks.

The Au content in native gold ranges from 90.15 wt% to 99.82 wt%, in addition to containing certain amounts of Ag (<7.51 wt%), Se (<4.56 wt%), and Hg (<7.02 wt%) (Table 1). Additionally, because of the high organic carbon content in the rocks and ores of the La’erma mine, some gold is adsorbed in kerogen, reaching levels as high as 116 ppm [36].

Table 1. Major element compositions of native gold, selenides, and sulfides from the La’erma and Qiongmo Au–Se deposits (wt%).

Minerals	Native Gold	Tiemannite	Antimonelite *	Clausthalite	Kullerudite	Ni ₃ As ₃ S ₃ Se	Se-Bearing Stibnite *	Se-Bearing Famatinite	Se-Bearing Pyrite
Au	90.15~99.82								
Ag	0.00~7.51					0.03		0.00~0.33	
Hg	0.00~7.02	67.04~77.20	0.00~3.69	0.23~4.97	0.32~2.16	5.36	0.00~2.08	0.00~1.49	
Sb		0.00~0.18	48.94~59.13				58.47~72.99		5.40~8.07
Pb				71.79~77.83					
Ni					24.80~27.71	29.38	0.00~0.11		3.97~4.59
As						33.90		0.00~2.01	
Fe					0.35~3.17	0.23	0.00~0.05		32.42~33.50
Cu						0.46		36.60~39.94	
Zn							0.00~0.44		
Se	0.00~4.56	17.73~33.01	29.20~46.86	16.79~25.19	67.67~73.06	12.67	0.00~29.12	6.11~23.89	19.71~22.61
S		0.44~5.18	1.99~11.43	0.23~4.97	0.09~0.72	15.56	11.86~28.76	14.49~25.74	32.86~35.27

* EPMA analysis results come from Liu and Zheng [47] and Liu et al. [48].

4.2. Selenides

The La’erma and Qiongmo Au–Se deposits contain Se in three forms: independent selenides, isomorphism in Se-bearing sulfides, and adsorption (Figures 5–8) [15,44]. Similarly to native gold, selenides are also produced in the form of associated selenides, intergranular selenides, fissure selenides, and encapsulated selenides. The associated selenides often coexist with native gold and stibnite. Selenides can also occupy the spaces between quartz, baryte, and stibnite particles, appearing as fine veins and veinlets in quartz and baryte fissures. At the same time, selenides are often encapsulated in minerals such as stibnite, quartz, baryte, and dickite, which encapsulate selenium (Figure 5).

A variety of independent selenides are reported in the La’erma and Qiongmo deposits, including tiemannite (HgSe), antimonelite (Sb₂Se₃), clausthalite (PbSe), kullerudite (NiSe₂), and an unnamed Ni₃As₃S₃Se mineral phase.

Tiemannite (HgSe) is widely distributed in the deposit, where it is deposited in stage II. The tiemannite is irregular, ranging in size from 10 to 50 μm. It often coexists with native gold, stibnite, famatinite, sphalerite, and antimonelite (Figures 5 and 7). The EPMA data results for the tiemannite showed that it was composed of Hg and Se, with content ranging from 67.04% to 77.20 wt% and 17.73% to 33.01 wt% (Table 1), respectively. Small amounts of S and Sb are present, with content ranges of 0.44%–5.18 wt% and 0.00%–0.183 wt%, respectively. The calculated mean formula of tiemannite is Hg_{0.92}(Se_{0.95},S_{0.05})_{1.00} or simply Hg(Se, S). The range of SeS₋₁ substitution is 0.58–1.00 *apfu* in tiemannite (Figure 9a).

The antimonelite (Sb₂Se₃) is anhedral with particle sizes of 2–40 μm (Figure 5). Antimonelite is intergrown with tiemannite, clausthalite, and Se-bearing stibnite (Figure 7). The Sb, Se, and S content ranges in antimonelite are 48.94–59.13 wt%, 29.20–46.86 wt%, and 1.99–11.43 wt%, respectively. The range of SeS₋₁ substitution is larger in antimonelite (up to 0.91 *apfu*) than in the case of Se-bearing stibnite with contents up to 0.48 *apfu* (Figure 9b). Clausthalite (PbSe) contains 71.79–77.83 wt% Pb and 16.79–25.19 wt% Se, with traces of S (0.23–4.97 wt%) and Hg (0.23–4.97 wt%). In general, the kullerudite (NiSe₂) coexisting with baryte and stibnite is granular or acicular. The kullerudite is steel-gray and strongly inhomogeneous. Major element compositions of kullerudite showed that Ni varied from 24.80 wt% to 27.71 wt%, and Se ranged from 67.67 wt% to 73.06 wt%. On the basis of the average microprobe analyses, the calculated mean formulas of antimonelite, clausthalite, and kullerudite are (Sb_{1.92},Hg_{0.03})_{1.95}(Se_{2.13},S_{0.87})_{3.00}, Pb_{1.00}(Se_{0.81},S_{0.19})_{1.00},

and $(\text{Ni}_{1.00}\text{Fe}_{0.04})_{1.04}(\text{Se}_{1.98}\text{S}_{0.03})_{2.01}$, respectively. The anhedral granular $\text{Ni}_3\text{As}_3\text{S}_3\text{Se}$ mineral phase with $< 10 \mu\text{m}$ contains 29.38 wt% Ni, 33.90 wt% As, 15.56 wt% S, and 12.67 wt% Se with traces of Hg. The calculated mean formula of $\text{Ni}_3\text{As}_3\text{S}_3\text{Se}$ mineral phase is $\text{Ni}_{3.20}\text{As}_{2.82}\text{S}_{3.03}\text{Se}_{1.00}$.

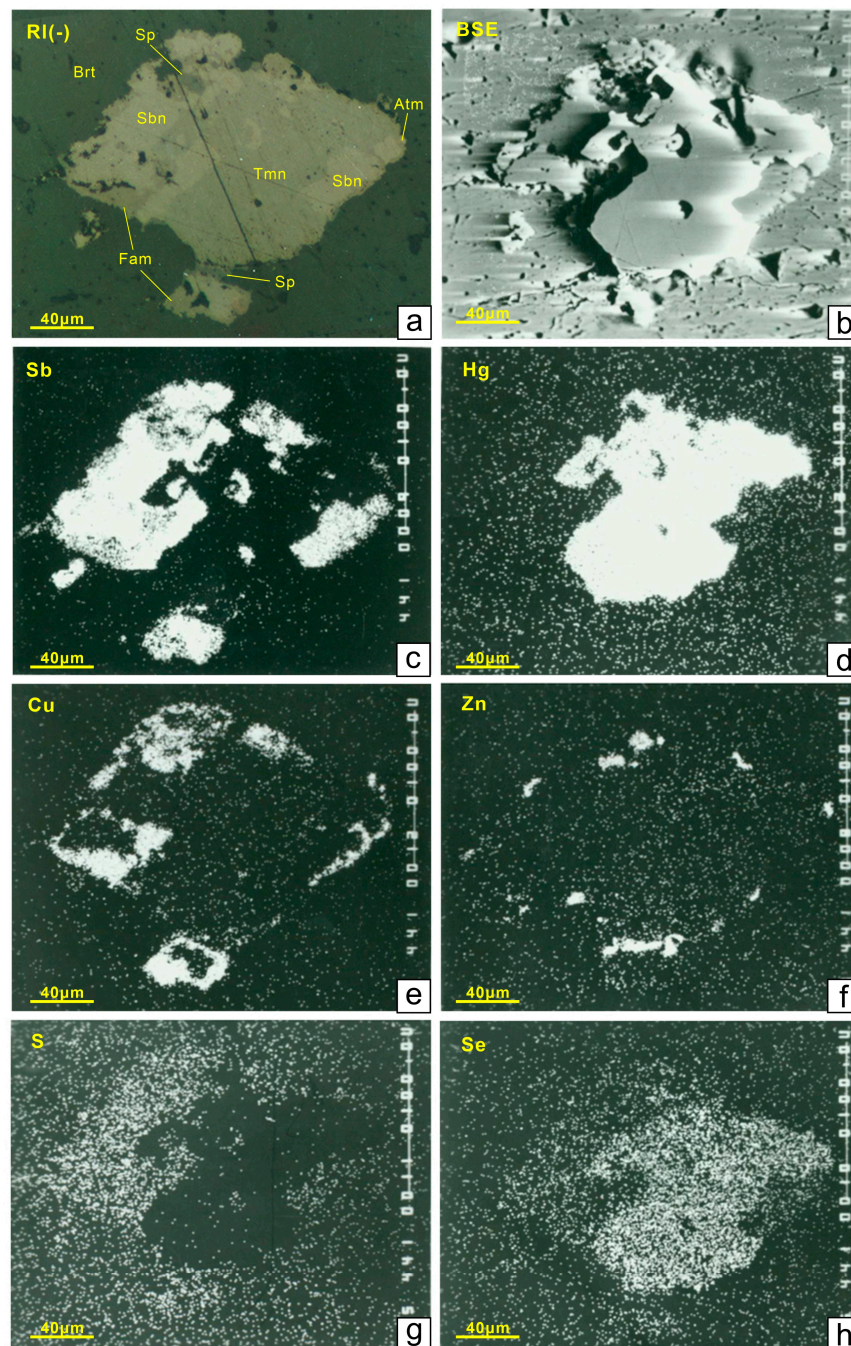


Figure 7. (a) Micrograph of mineral assemblages of tiemannite, antimonselite, and stibnite; (b) back-scattered electron (BSE) images; (c–h) element maps for Sb, Hg, Cu, Zn, S, and Se showing independent selenides and isomorphism in Se-bearing sulfides. Abbreviations: Tmn = tiemannite; Sbn = stibnite; Atm = antimonselite; Fam = famatinite; Sp = sphalerite.

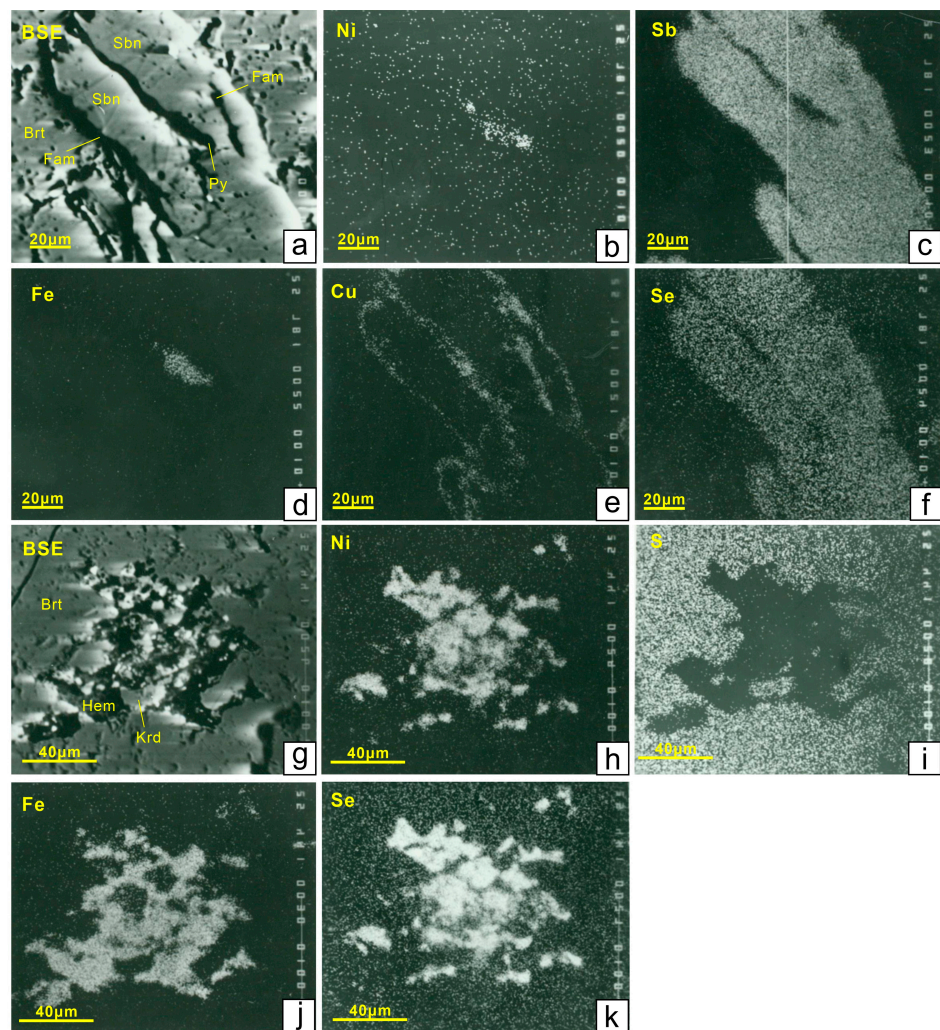


Figure 8. (a) Back-scattered electron (BSE) images for pyrite, famatinite, and stibnite; (c–h) element maps for Ni, Sb, Fe, Cu, and Se showing Se entered the mineral lattice by replacing S; (g) back-scattered electron (BSE) images for kullerudite; (h–k) element maps for Ni, S, Fe, and Se showing uniform element distribution. Abbreviations: Py = pyrite; Sbn = stibnite; Fam = famatinite; Krd = kullerudite; Hem = hematite; Brt = baryte.

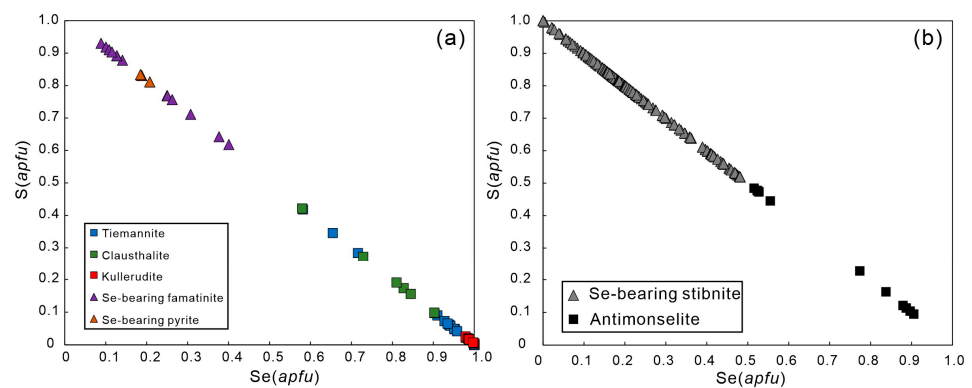


Figure 9. Graph of Se vs. S (apfu) for selenides and Se-bearing sulfides from the La’erma and Qiongmo Au–Se deposits. (a) Se vs. S (apfu) plot for tiemannite, clausthalite, kullerudite, Se-bearing famatinite and Se-bearing pyrite; (b) Se vs. S (apfu) plot for antimonelite and Se-bearing stibnite.

4.3. Se-Bearing Sulfides

In addition to the independent selenides described above, selenium can often replace sulfur in sulfides because of their similar crystallochemical properties [3]. Several sulfides, which include stibnite, pyrite, marcasite, tetrahedrite, sphalerite, and cinnabar in the La'erma and Qiongmo Au–Se deposits, contain selenium (Figures 7 and 8). The main sulfides containing selenium are stibnite, famatinite, and pyrite (Table 1). Among these sulfides, stibnite has the highest Se content, with a Se content variation ranging from 8.42 to 25.41 wt%. The Se-bearing famatinite contains 6.11–23.89 wt% Se and 14.49.65–25.74 wt% S. The Fe, Se, and S content ranges in Se-bearing pyrite are 32.42–33.50 wt%, 19.71–22.61 wt% and 32.86–35.27 wt%. The calculated mean formulas of Se-bearing stibnite, Se-bearing famatinite, and Se-bearing pyrite are $Sb_{2.02}(Se_{0.63},S_{2.37})_{3.00}$, $Cu_{2.88}Sb_{1.04}(S_{3.20},Se_{0.80})_{4.00}$, and $(Fe_{0.87},Sb_{0.09},Ni_{0.11})_{1.87}(S_{1.61}Se_{0.39})_{2.00}$, respectively. Liu et al. [35] found that the Se content is closely related to the organic carbon content, meaning that this portion of Se is present in the form of adsorbed Se.

5. Discussion

5.1. Physicochemical Conditions of Mineral Deposition

In the La'erma and Qiongmo Au–Se deposits, orebodies are found in carbonaceous cherts and slates, and the boundary between the orebody and the host rocks is indistinct. A combination of medium- and low-temperature hydrothermal minerals has formed. Therefore, the La'erma and Qiongmo Au–Se deposits are classified as Carlin-type gold deposits due to their characteristics [46].

To decipher the solution speciation, fluid evolution processes, and mechanisms for mineral precipitation, we studied the physicochemical conditions of ore-forming fluids [49]. The La'erma and Qiongmo Au–Se deposits have undergone significant changes in mineral composition during their two main metallogenic stages. Stage II is dominated by sulfides, while stage III is dominated by selenides, indicating significant changes in the physicochemical conditions of these two stages. This allows us to conveniently investigate the physicochemical conditions of mineral precipitation during the main metallogenic stages (stages II and III). The phase stability of the main minerals were calculated using HSC Chemistry 6.0 with the thermodynamic properties from previous studies [3,50,51].

Fugacity–temperature diagrams show the relative tendency of various metals to form sulfides and selenides, which can reflect the conditions of ore formation. Both main mineralization stages contain stibnite, resulting in minimal changes to sulfur fugacity (Figure 10a). However, the selenium fugacity exhibited a significant increase (Figure 10b). This change is in line with the absence of selenide in stage II and the significant precipitation of selenide in stage III.

In stage II, fluid inclusions in quartz and baryte have a homogenization temperature range of 222–269 °C, with average temperature of 242 °C [15]. Sulfur fugacity ($\log f_{S_2}$) can be defined by the characteristic mineral assemblages of stibnite–polydymite–pyrrhotite–galena–baryte. Therefore, $\log f_{S_2}$ values ranged from -10.44 to -14.60 at 242 °C (Figure 11a). Comparably, the homogenization temperature of fluid inclusions in quartz and baryte of stage III has decreased, with a range of 142–265 °C and average temperature of 197 °C [15]. $\log f_{S_2}$ values that ranging from -7.13 to -12.20 were estimated in stage III due to the presence of a paragenetic association consisting of stibnite, vaesite, galena, baryte, and the absence of polydymite (Figure 11b).

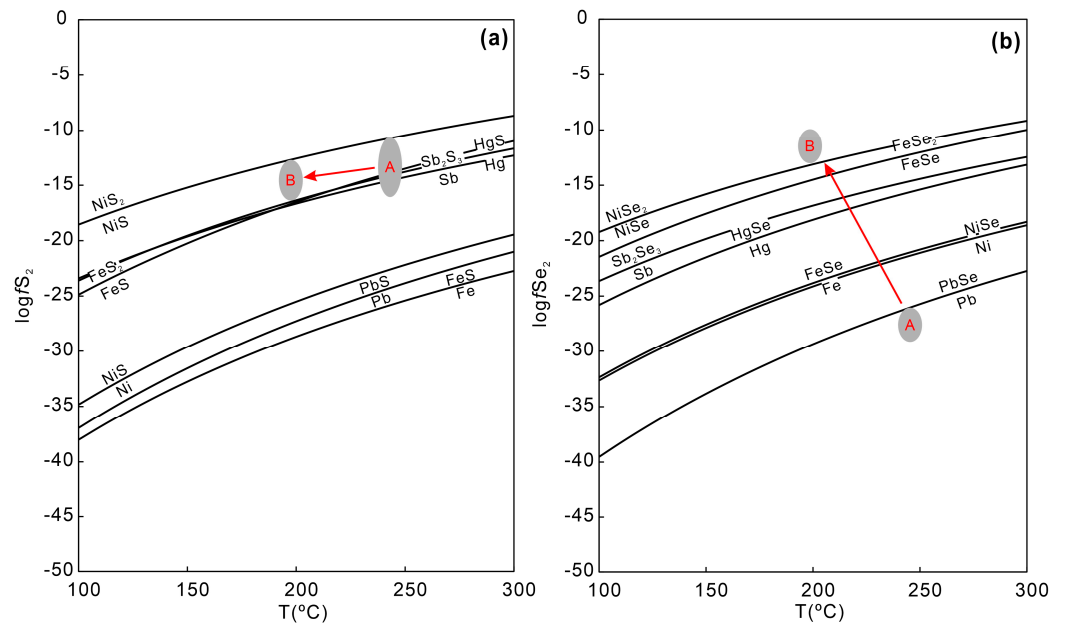
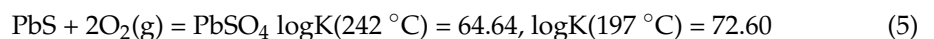
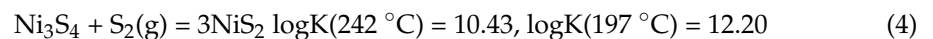
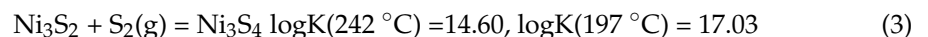
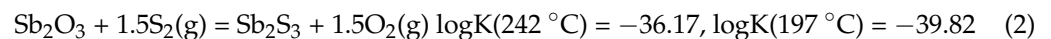


Figure 10. (a) $\log f_{S_2}$ -T diagram different reactions as a function of temperature ($^{\circ}\text{C}$) and sulfur fugacity; (b) $\log f_{Se_2}$ -T diagram different reactions as a function of temperature ($^{\circ}\text{C}$) and selenium fugacity (modified from Simon et al. [3]). A and B represent the sulfur fugacity and selenium fugacity and temperature range corresponding to mineral assemblages at different stages. Here, A represents the sulfide assemblage in stage II, while B represents selenides assemblages in stage III.

The following reactions were considered possible mineral deposition processes:



We also estimated changes in Se fugacity ($\log f_{Se_2}$) in the La'erma and Qiongmo Au-Se deposits based on the precipitation of a large number of selenides. In stage II, there are paragenetic associations of stibnite-galena-pyrite-pyrrhotite-sphalerite but no selenides. The $\log f_{Se_2}$ - $\log f_{S_2}$ phase diagram further constrains the range of Se fugacity ($\log f_{Se_2} < \log f_{S_2} - 1.92$), and the upper limit of $\log f_{Se_2}$ was estimated to be -10.70 (Figure 11c). The occurrence of antimonite-stibnite, kullerudite-vaesite, native gold, clausthalite, and tiemannite, as well as the absence of AuSe, defines the $\log f_{Se_2}$ ranging from -13.98 to -8.82 , which is required to precipitate a large number of selenides in stage III (Figure 11d). In addition, we believe that the Se fugacity decreased significantly due to a large amount of selenide precipitation, causing sulfides such as cinnabar, realgar, and orpiment to precipitate again in the late stage III (Figure 11d).

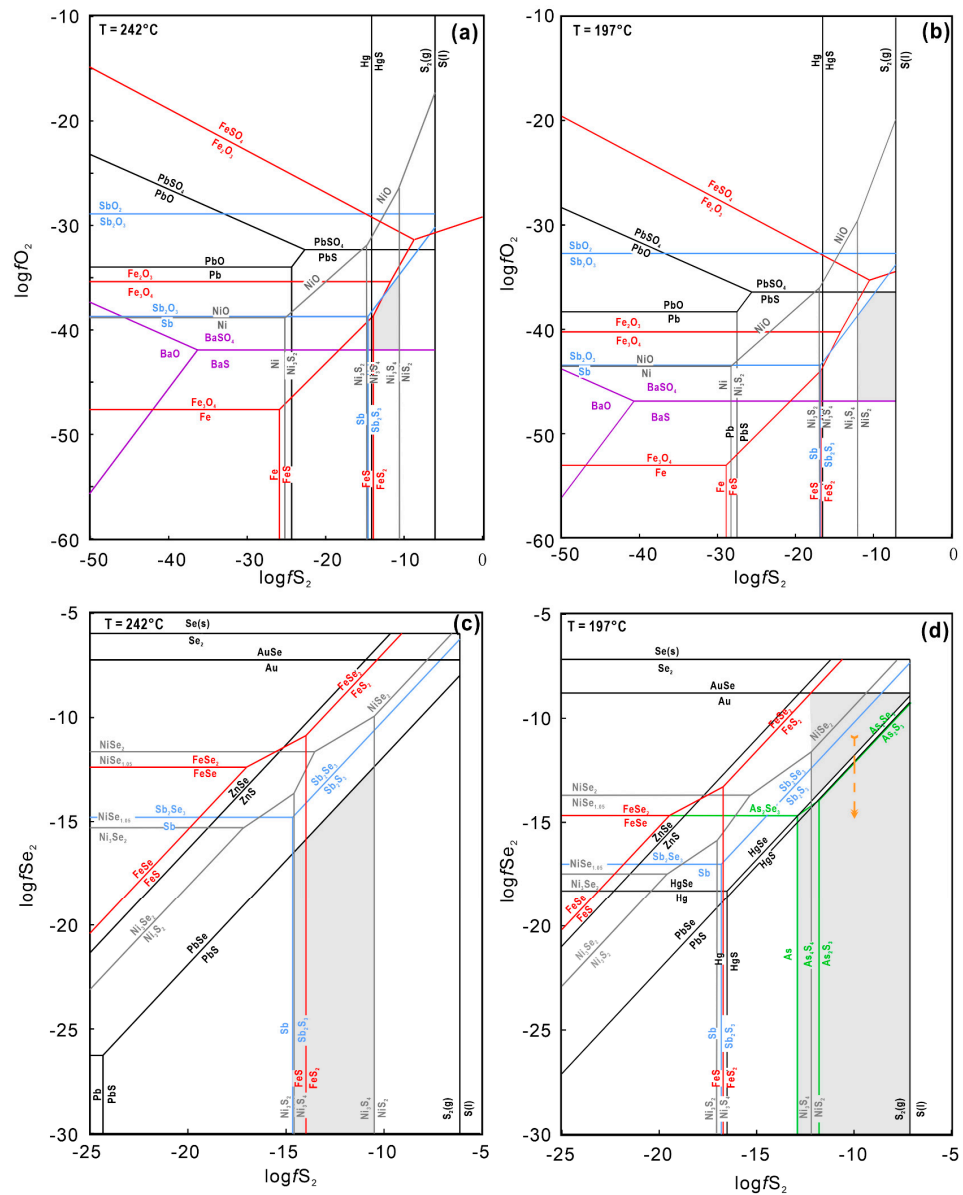
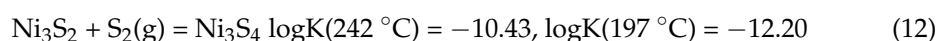
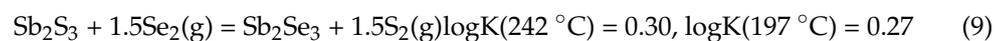
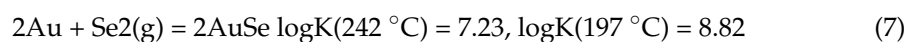


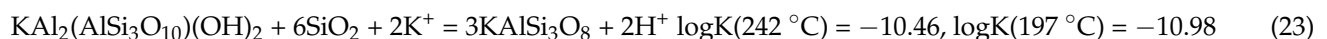
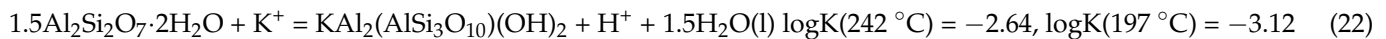
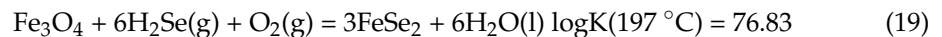
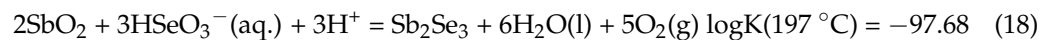
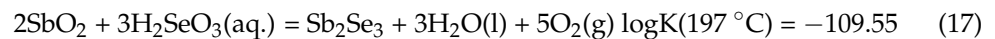
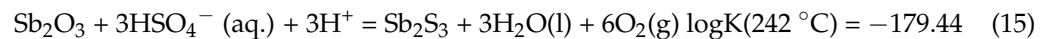
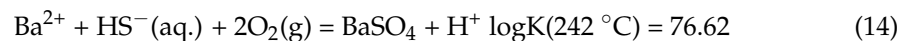
Figure 11. (a) LogfS₂—logfO₂ diagram showing the stability of some sulfides and their corresponding oxides from stage II at 242 °C; (b) LogfS₂—logfO₂ diagram showing the stability of some sulfides and their corresponding oxides from stage III at 197 °C; (c) LogfSe₂—logfS₂ diagrams showing the fields of stability for some selenides and their corresponding sulfides from stage II at 242 °C (modified from Simon and Essene [50]); (d) LogfSe₂—logfS₂ diagrams showing the fields of stability for some selenides and their corresponding selenides from stage III at 197 °C (modified from Simon and Essene [50]).

Reactions related to selenides are as follows:



Because selenides typically precipitate in a relatively oxidizing condition [3,10], it is important to study changes in oxygen fugacity ($\log f_{O_2}$) in the La'erma and Qiongmo Au–Se deposits. The coexistence of stibnite and baryte is a significant feature of stage II. Since sulfides are predominantly present during this stage, we used the Fe–Cu–Sb–S–O system and overlaid the stability domain of baryte to determine the oxygen fugacity of Stage II (Figure 12). It was assumed that the pH ranged from 4.64 to 7.23 in stage II due to the widespread presence of “sericite” and the absence of “dickite” in the deposit (Figure 11a). Correspondingly, the oxygen fugacity was constrained between -32.78 and -39.43 (Figure 11a). The abundance of selenides in stage III suggests that the M (Fe, Sb, Ni, Hg, Pb, etc.)–Se–O system was better suited for controlling oxygen fugacity than the Fe–Cu–Sb–S–O system (Figure 12b). The oxygen fugacity in La'erma, as determined by the paragenetic associations of selenides, was between -28.28 and -40.83 (Figure 12b). The acidic ore-forming fluid ($\text{pH} < 4.64$) of stage III meets the requirements for dickite (Figure 12b).

In the process, the following reactions restrict the range of physicochemical conditions:



5.2. Reasons for Se-Enrichment

Although tellurides are more abundant than selenides in mineral deposits, Se has a higher content in the crust compared to Te [52]. This is because stricter physicochemical conditions are required for the precipitation of independent selenides. In general, a high oxidizing condition is crucial for the formation of selenides, just like selenium mineralization in the Příbram Uranium and BaseMetal District [53]. When Se is prevented from entering sulfides due to the formation of SO_4^{2-} in relatively oxidizing condition, it promotes the precipitation of selenides instead of replacing sulfur in sulfides [3,15]. Fluids can become oxidized through boiling or the addition of oxidizing fluid [54–56].

Previous studies have shown that significant boiling of ore-forming fluids occurred during the mineralization process of the La'erma and Qiongmo Au–Se deposits [35], which led to the loss of H_2S and an increase in the $\text{SO}_4^{2-}/\text{H}_2\text{S}$ ratio, resulting in the relative oxidation of the ore-forming fluids. Furthermore, the hydrothermal fluids at the La'erma and Qiongmo Au–Se deposits have been mixed with oxidizing meteoric water [57]. In both stages II and III, the ore-forming environments had a relatively high oxygen fugacity. This is consistent with the significant amount of baryte precipitation in the mining area. The oxidation of the ore-forming condition can effectively remove Au from fluids (Figure 12a) [58].

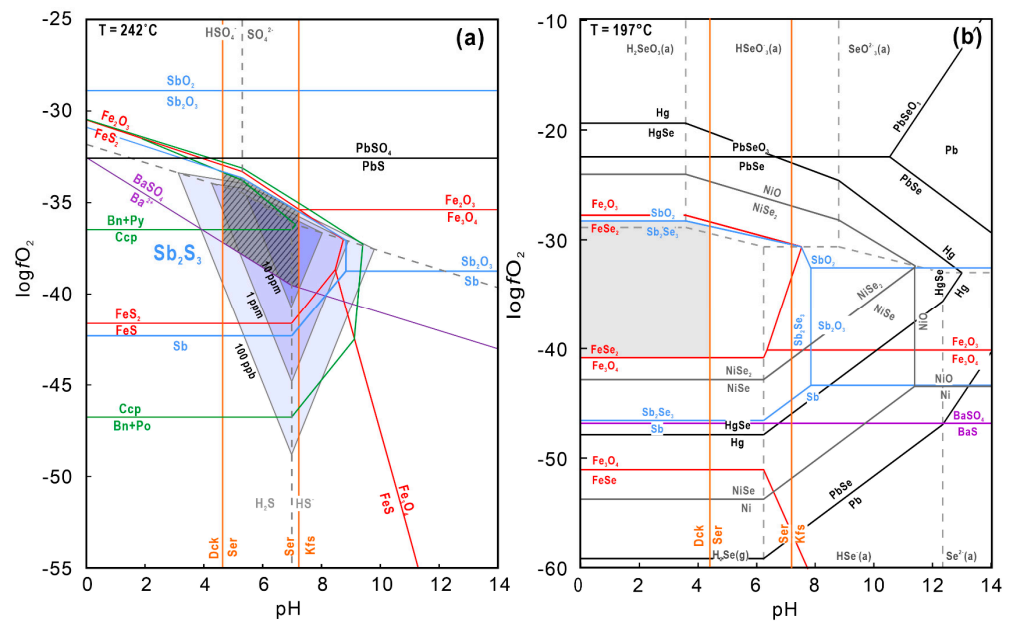
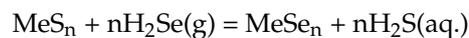


Figure 12. (a) At 242 °C, a LogfO₂(g) vs. pH diagram for Fe–Cu–Sb–S–O is plotted. Additionally, the stability fields of baryte are indicated in the shadow region, with the purple region showing gold solubility (modified by Williams-Jones et al. [58]); (b) At 197 °C, a LogfO₂(g) vs. pH diagram for M (Fe, Sb, Ni, Hg, Pb, etc.)–Se–O system is plotted with the stability fields of baryte. Abbreviations: Bn = bornite; Ccp = chalcopyrite; Py = pyrite; Dck = dickite; Ser = sericite; Kfs = K-feldspar.

However, the different stages of oxygen fugacity obtained from various mineral combinations indicate that at 197 °C, stage III, which is characterized by a significant amount of selenide precipitation, had a lower oxygen fugacity than stage II, which is dominated by sulfide precipitation (Figure 12b). The statement appears to contradict the notion that the precipitation of selenides is controlled by the oxidation environment. We consider that the deposition of selenide was controlled by the high ΣSe/S ratio of the hydrothermal fluid, while a high oxygen fugacity mineralization environment is only a basic condition [59].

There is a potential use of simple mineral pairs such as metallic (Me) sulfides and metallic (Me) selenides in an ideal solid solution to estimate the ΣSe/S ratio in the fluid [60]. At 242 °C, H₂S is the dominant aqueous S species, while at 197 °C, H₂Se is the dominant aqueous Se species, as shown in Figure 12. Therefore, the universal reaction equation is as follows:



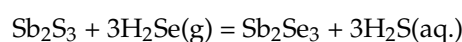
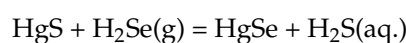
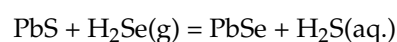
The law of mass action implies that for the MeS_n – MeSe_n reaction:

$$\log K_{\text{reaction}} = \log (\alpha_{\text{MeSe}_n} / \alpha_{\text{MeS}_n}) - n \log (\alpha_{\text{H}_2\text{Se}} / \alpha_{\text{H}_2\text{S}})$$

where $\alpha_{\text{H}_2\text{Se}} / \alpha_{\text{H}_2\text{S}}$ approximates to $m_{\text{H}_2\text{Se}} / m_{\text{H}_2\text{S}}$ in aqueous fluids [60], and the activity (α) equals the mole fraction (X) for ideal solid solutions [50,60]; hence:

$$\log K_{\text{reaction}} = \log (X_{\text{MeSe}_n} / X_{\text{MeS}_n}) - n \log (m_{\text{H}_2\text{Se}} / m_{\text{H}_2\text{S}})$$

The reactions involved are as follows:



The elemental content of selenides (clausthalite, tiemannite, and antimonelite) from previous studies was utilized [11,24,61], and a Se content of 0.1 wt% was assumed for Se-depleted sulfides which are considered from stage II. Based on these data, the ratio of $\text{H}_2\text{Se}/\text{H}_2\text{S}$ in the fluid was calculated. For PbS–PbSe mineral pairs, the ratio of $\text{H}_2\text{Se}/\text{H}_2\text{S}$ in the fluid that precipitated the PbSe representing stage III was two orders of magnitude higher than that in the fluid that precipitated the PbS representing stage II (path A; Figure 13).

Conversely, in the mineral pair HgS–HgSe, a two orders of magnitude decrease in the Se/S ratio resulted in the transition from tiemannite to cinnabar during the late stage III (path B; Figure 13). This decrease can be attributed to a significant amount of selenide precipitates, which caused a rapid decrease in Se fugacity and resulted in the precipitation of Hg and As in the form of cinnabar, realgar, and orpiment. Figure 13 also shows that the precipitation of antimonelite requires a more extreme $\Sigma\text{Se}/\text{S}$ ratio compared to other selenides. According to Kolova et al. [62], the precipitation of selenides is caused by decreasing sulfur and increasing selenium contents, resulting in an increase in $\Sigma\text{Se}/\text{S}$ ratio.

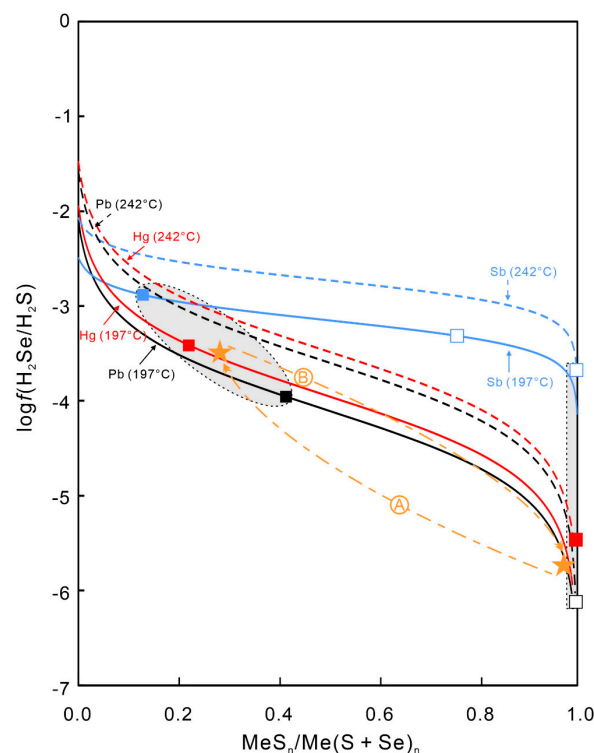


Figure 13. The $\log f(\text{H}_2\text{Se}/\text{H}_2\text{S})$ vs. $\text{MeS}_n/\text{Me}(\text{S} + \text{Se})_n$ diagram showing the relation between $\Sigma\text{Se}/\text{S}$ ratio and the mole fraction in an ideal solid solution for $\text{Me}(\text{Pb}, \text{Hg}, \text{Sb})(\text{Se}, \text{S})$ (modified by Huston et al. [60]). A and B represent the range of $\log f(\text{H}_2\text{Se}/\text{H}_2\text{S})$ and $\text{MeS}_n/\text{Me}(\text{S} + \text{Se})_n$ changes corresponding to mineral in different stages. Here, path A represents the changes in $\log f(\text{H}_2\text{Se}/\text{H}_2\text{S})$ when $\text{PbS} + \text{Sb}_2\text{S}_3$ mineral assemblages of stage II transforms into $\text{PbSe} + \text{Sb}_2\text{Se}_3$ mineral assemblages of stage III, while path B represents the changes in $\log f(\text{H}_2\text{Se}/\text{H}_2\text{S})$ when HgSe transforms into HgS in stage III.

In summary, the precipitation of selenide was ultimately controlled by the high $\Sigma\text{Se}/\text{S}$ ratio in the hydrothermal fluid. The range of S isotopes in the main sulfides and sulfates of the La'erma and Qiongmo Au–Se deposits varied widely, which is consistent with the siliceous formation of Cambrian age [42]. This suggests that the ore-forming materials were derived from the Se-rich siliceous strata. The H–O isotopic composition during the main metallogenic stage suggests that the fluid was derived from groundwater replenished by meteoric water, and that there was a significant water–rock reaction between the ore-forming fluid and host rocks [57]. Therefore, in a relatively oxidizing environment, Se was

introduced through water–rock reactions from Se-rich siliceous formations. This resulted in an increase in the $\Sigma\text{Se}/\text{S}$ ratio of the fluid and the deposition of special Au–Se deposits.

6. Conclusions

1. The La'erma and Qiongmo Au–Se deposits developed a variety of selenides, native gold, and stibnite that coexist with baryte. Based on the mineral assemblage and metallogenic temperature, the $\log f\text{S}_2$ values of the sulfide assemblage at stage II probably ranged between -10.44 and -14.60 with $\log f\text{Se}_2$ being less than -10.70 . Comparably, during stage III, which is characterized by many selenides, the $\log f\text{S}_2$ and $\log f\text{Se}_2$ ranged from -7.13 to -12.20 and -13.98 to -8.82 , respectively.
2. The redox conditions were consistently oxidizing, as confirmed by the persistent presence of baryte. However, the oxidizing condition was only a fundamental prerequisite for selenides' deposition. The ultimate controlling factor for the precipitation of selenides was a high $\Sigma\text{Se}/\text{S}$ ratio of the fluid. Simulations of phase diagrams revealed that an increase in the $\Sigma\text{Se}/\text{S}$ ratio of the fluid through water–rock reactions promoted the precipitation of selenides rather than sulfides.

Author Contributions: Conceptualization, J.L. and G.W.; methodology, J.L., D.Z. and G.W.; writing—original draft preparation, J.L. and G.W.; validation, Y.W., F.Z. and S.G.; writing—review and editing, E.J.M.C., G.W. and L.X. All authors have read and agreed to the published version of the manuscript.

Funding: This research was funded by the Major Research Plan of National Natural Science Foundation of China, grant No. 92062219.

Data Availability Statement: The dataset is presented directly in the present study.

Conflicts of Interest: The authors declare no conflicts of interest.

References

1. Rudnick, R.L.; Gao, S. Composition of the continental crust. *Treatise Geochem.* **2003**, *3*, 659.
2. Hu, Z.C.; Gao, S. Upper crustal abundances of trace elements: A revision and update. *Chem. Geol.* **2008**, *253*, 205–221. [[CrossRef](#)]
3. Simon, G.; Kesler, S.E.; Essene, E.J. Phase relations among selenides, sulfides, tellurides and oxides: II. applications to selenide-bearing ore deposits. *Econ. Geol.* **1997**, *92*, 465–484. [[CrossRef](#)]
4. Zhai, D.G.; Williams-Jones, A.E.; Liu, J.J.; Tombros, S.F.; Cook, N.J. Mineralogical, fluid inclusion, and multiple isotope (H-O-S-Pb) constraints on the genesis of the Sandaowanzi epithermal Au-Ag-Te Deposit, NE China. *Econ. Geol.* **2018**, *113*, 1359–1382. [[CrossRef](#)]
5. Wang, D.Z.; Zhen, S.M.; Liu, J.J.; Carranza, E.J.M.; Wang, J.; Zha, Z.J.; Li, Y.S.; Bai, H.J. Mineral paragenesis and hydrothermal evolution of the Dabaiyang tellurium-gold deposit, Hebei Province, China: Constraints from fluid inclusions, H-O-He-Ar isotopes, and physicochemical conditions. *Ore Geol. Rev.* **2021**, *130*, 103904. [[CrossRef](#)]
6. Zhu, J.; Zuo, W.; Liang, X.; Li, S.; Zheng, B. Occurrence of native selenium in Yutangba and its environmental implications. *Appl. Geochem.* **2004**, *19*, 461–467. [[CrossRef](#)]
7. So, C.S.; Dunchenko, V.Y.; Yun, S.T.; Park, M.E.; Choi, S.G.; Shelton, K.L. Te- and Se-bearing epithermal Au-Ag mineralization, Prasolovskoye, Kunashir Island, Kuril island arc. *Econ. Geol.* **1995**, *90*, 105–117. [[CrossRef](#)]
8. Finkelman, R.B.; Mrose, M.E. Downeyite, the first verified natural occurrence of SeO_2 . *Am. Mineral.* **1977**, *62*, 316–320.
9. Luo, K.D.; Wei, J.; Zhang, J.Y.; Gu, Q.F. Chalcomenite—A new selenous acid oxysalts mineral. *Chin. Sci. Bull.* **1980**, *2*, 85–89. (In Chinese)
10. Weng, G.M.; Liu, J.J.; Carranza, E.J.M.; Zhai, D.G.; Zhang, F.F.; Wang, Y.H.; Yu, C.; Zhang, B.; Liu, X.H.; Sun, B.; et al. Mineralogy and geochemistry of tellurides, selenides and sulfides from the Zhaishang gold deposit, western Qinling, China: Implications for metallogenic processes. *J. Asian Earth Sci.* **2023**, *244*, 105536. [[CrossRef](#)]
11. Liu, J.J.; Zheng, M.H. First discovery of a compound in the antimony selenium-sulfur series. *Chin. Sci. Bull.* **1992**, *9*, 864. (In Chinese)
12. Wang, X.; Liu, J.; Carranza, E.J.M.; Zhai, D.G.; Zhao, Q.Q.; Weng, G.M.; Zhang, B. Characteristics and formation conditions of Se-Bearing metacinnabar in the Wanshan mercury ore field, eastern Guizhou. *Minerals* **2023**, *13*, 173. [[CrossRef](#)]
13. Shao, Y.J.; Wang, W.S.; Liu, Q.Q.; Zhang, Y. Trace element analysis of pyrite from the Zhengchong gold deposit, northeast Hunan province, China: Implications for the ore-forming process. *Minerals* **2018**, *8*, 262. [[CrossRef](#)]
14. Beliaeva, T.V.; Palyanova, G.A. Silver Sulfides and Selenides in Ores from Au–Ag Epithermal Deposits of the Okhotsk–Chukotka Volcanic Belt. *Geol. Ore Depos.* **2023**, *65*, 72–105. [[CrossRef](#)]
15. Liu, J.J.; Zheng, M.H.; Liu, J.M.; Su, W.C. Geochemistry of the La'erma and Qiongmo Au–Se deposits in the western Qinling Mountains, China. *Ore Geol. Rev.* **2000**, *17*, 91–111. [[CrossRef](#)]

16. Sidorov, E.G.; Borovikov, A.A.; Tolstykh, N.D.; Bukhanova, D.S.; Palyanova, G.A.; Chubarov, V.M. Gold mineralization at the maletoyvayam deposit (Koryak Highland, Russia) and physicochemical conditions of its formation. *Minerals* **2020**, *10*, 1093. [[CrossRef](#)]
17. Kovalenker, V.A.; Plotinskaya, O.Y.; Prokof'ev, V.Y.; Pomortsev, V.V.; Koneev, R.I. Mineralogy, geochemistry, and genesis of gold-sulfide-selenide-telluride ores from the Kairagach deposit (Uzbekistan). *Geol. Ore Depos.* **2003**, *45*, 171–200.
18. Redwood, S.D. Famous mineral localities: The Pacajake selenium mine, Potosi, Bolivia. *Mineral. Rec.* **2003**, *34*, 339.
19. Hans-Jürgen, F.; Luca, B.; Chris, J.S. Grundmannite, CuBiSe₂, the Se-analogue of emplectite, a new mineral from the El Dragon mine, Potosi, Bolivia. *Eur. J. Mineral.* **2016**, *28*, 467–477. [[CrossRef](#)]
20. Song, C.Z. A brief description of the Yutangba sedimentary type selenium mineralized area in southwestern Hubei. *Miner. Depos.* **1989**, *3*, 83–89, (In Chinese with English Abstract).
21. Dai, S.F.; Yang, J.Y.; Ward, C.R.; Hower, J.C.; Liu, H.D.; Garrison, T.M.; French, D.; O'Keefe, J.M.K. Geochemical and mineralogical evidence for a coal-hosted uranium deposit in the Yili Basin, Xinjiang, northwestern China. *Ore Geol. Rev.* **2015**, *70*, 1–30. [[CrossRef](#)]
22. Dill, H.G. The “chessboard” classification scheme of mineral deposits: Mineralogy and geology from aluminum to zirconium. *Earth-Sci. Rev.* **2010**, *100*, 1–420. [[CrossRef](#)]
23. Saunders, J.A.; Brueseke, M.E. Volatility of Se and Te during subduction-related distillation and the geochemistry of epithermal ores of the western United states. *Econ. Geol.* **2012**, *107*, 165–172. [[CrossRef](#)]
24. Shuai, D.Q.; Hu, X.Q. Mineral component features and gold migration patterns of La'erma gold deposit in Gansu-Sichuan. *Geol. Explor.* **1995**, *31*, 28–35, (In Chinese with English Abstract).
25. Dong, Y.P.; Santosh, M. Tectonic architecture and multiple orogeny of the Qinling Orogenic Belt, Central China. *Gondwana Res.* **2016**, *29*, 1–40. [[CrossRef](#)]
26. Dong, Y.P.; Sun, S.S.; Santosh, M.; Zhao, J.; Sun, J.P.; He, D.F.; Shi, X.H.; Hui, B.; Cheng, C.; Zhang, G.W. Central China Orogenic Belt and amalgamation of East Asian continents. *Gondwana Res.* **2021**, *100*, 131–194. [[CrossRef](#)]
27. Zhang, G.W.; Guo, A.L.; Dong, Y.P.; Yao, A.P. Rethinking of the Qinling Orogen. *J. Geomech.* **2019**, *25*, 746–768, (In Chinese with English Abstract).
28. Dong, Y.P.; Zhang, G.W.; Neubauer, F.; Liu, X.M.; Genser, J.; Hauzenberger, C. Tectonic evolution of the Qinling orogen, China: Review and synthesis. *J. Asian Earth Sci.* **2011**, *41*, 213–237. [[CrossRef](#)]
29. Qiu, K.F.; Deng, J.; He, D.Y.; Rosenbaum, G.; Zheng, X.; Williams-Jones, A.E.; Yu, H.C.; Balen, D. Evidence of vertical slab tearing in the late triassic Qinling Orogen (central China) from multiproxy geochemical and isotopic imaging. *JCR Solid Earth* **2023**, *128*, e2022JB025514. [[CrossRef](#)]
30. Liu, J.J.; Dai, H.Z.; Zhai, D.G.; Wang, J.P.; Wang, Y.H.; Yang, L.B.; Mao, G.J.; Liu, X.H.; Liao, Y.F.; Yu, C.; et al. Geological and geochemical characteristics and formation mechanisms of the Zhaishang Carlin-like type gold deposit, western Qinling Mountains, China. *Ore Geol. Rev.* **2015**, *64*, 273–298. [[CrossRef](#)]
31. Zhang, G.W.; Zhang, B.R.; Yuan, X.C.; Xiao, Q.H. *Qinling Orogenic Belt and Continental Dynamics*; Science Press: Beijing, China, 2001; 855p. (In Chinese)
32. Meng, Q.R.; Zhang, G.W. Geologic framework and tectonic evolution of the Qinling orogen, central China. *Tectonophysics* **2000**, *323*, 183–196. [[CrossRef](#)]
33. Hu, F.Y.; Liu, S.W.; Ducea, M.N.; Chapman, J.B.; Wu, F.Y.; Kusky, T. Early Mesozoic magmatism and tectonic evolution of the Qinling Orogen: Implications for oblique continental collision. *Gondwana Res.* **2020**, *88*, 296–332. [[CrossRef](#)]
34. Liu, J.J.; Liu, J.M.; Zheng, M.H.; Liu, X.F. Au–Se paragenesis in Cambrian stratabound gold deposits, western Qinling Mountains, China. *Int. Geol. Rev.* **2000**, *42*, 1037–1045. [[CrossRef](#)]
35. Liu, J.J.; Zheng, M.H.; Liu, J.M. Selenium enrichment in Cambrian stratabound gold deposits in western Qinling Mountains: Characteristics, origin and prospects. *Acta Geol. Sin.* **1997**, *71*, 266–273. (In Chinese with English Abstract)
36. Liu, J.J.; Zheng, M.H. The gold occurrence of La'erma stratabound gold deposit. *Gold* **1994**, *15*, 7–12, (In Chinese with English Abstract).
37. Liu, J.J.; Zheng, M.H.; Liu, J.M.; Zhou, Y.F.; Gu, X.X.; Zhang, B. The geological and geochemical characteristics of Cambrian chert and their sedimentary environmental implications in western Qinling. *Acta Petrol. Sin.* **1999**, *15*, 145–154, (In Chinese with English Abstract).
38. Xu, L. Geological, Geochemical Characteristics and Genesis of the La'erma Gold Deposit in Gansu Province. Ms.D. Thesis, China University of Geosciences, Beijing, China, 2020.
39. He, W.M.; Li, W.J.; Ning, J.W.; Li, D.Z.; Wang, H.K. The geological characteristics and ore-controlling factors of La'erma gold deposit in Luqu county, Gansu province. *Miner. Resour. Geol.* **2017**, *31*, 99–105, (In Chinese with English Abstract).
40. Mao, J.W.; Qiu, Y.M.; Goldfarb, R.J.; Zhang, Z.C.; Garwin, S.; Fengshou, R. Geology, distribution, and classification of gold deposits in the western Qinling belt, central China. *Mineral. Depos.* **2002**, *37*, 352–377. [[CrossRef](#)]
41. Chen, Y.Y. Ore prospecting indicator and exploration model of gold deposits in South Gansu: Comparative analysis of Dashui, Zaozigou and La'erma gold deposits. *Miner. Resour. Geol.* **2020**, *34*, 7–18, (In Chinese with English Abstract).
42. Liu, J.J.; Zheng, M.H.; Liu, J.M.; Zhou, D.A. Sulfur isotopic composition and its geological significance of the Cambrian gold deposits in western Qinling, China. *J. Chang. Univ. Sci. Technol.* **2000**, *30*, 150–156, (In Chinese with English Abstract).

43. Liu, J.J.; Zheng, M.H.; Liu, J.M.; Lu, W.Q. A description of possible new Ni-As-S-Se mineral phase. *Acta Mineral. Sin.* **1995**, *15*, 425–427, (In Chinese with English Abstract).
44. Wen, H.J.; Qiu, Y.Z. Study on the organic/inorganic combined states of elements and the occurrence state of selenium in the La'erma Au–Se deposit. *Sci. China (Ser. D)* **1999**, *29*, 426–432. (In Chinese)
45. Liu, J.J.; Liu, C.H.; Wang, J.P.; Zhu, L.M. Classification and mineralization of the gold deposits in the western Qinling region, China. *Earth Sci. Front.* **2019**, *26*, 1–16, (In Chinese with English Abstract).
46. Liu, J.J.; Zhai, D.G.; Wang, D.Z.; Gao, S. Classification and mineralization of the Au-(Ag)-Te-Se deposits. *Earth Sci. Front.* **2020**, *27*, 79–98. (In Chinese with English Abstract)
47. Liu, J.J.; Zheng, M.H. The first discovery of selenio-sulfantimonide mineral series. *Chin. Sci. Bull.* **1992**, *37*, 1495–1496.
48. Liu, J.J.; Liu, J.M.; Liu, C.Q.; Lu, W.Q.; Liu, S.R.; Su, W.C. Mineralogy of the stibnite-antimonite series. *Int. Geol. Rev.* **1999**, *41*, 1042–1050.
49. Wood, M.J. Viral infections in neutropenia—Current problems and chemotherapeutic control. *J. Antimicrob. Chemoth.* **1998**, *41*, 81–93. [[CrossRef](#)] [[PubMed](#)]
50. Simon, G.; Essene, E.J. Phase relations among selenides, sulfides, tellurides, and oxides; I, Thermodynamic properties and calculated equilibria. *Econ. Geol.* **1996**, *91*, 1183–1208. [[CrossRef](#)]
51. Shock, E.L.; Helgeson, H.C.; Sverjensky, D.A. Calculation of the thermodynamic and transport properties of aqueous species at high pressures and temperatures: Standard partial molal properties of inorganic neutral species. *Geochim. Cosmochim. Acta* **1989**, *53*, 2157–2183. [[CrossRef](#)]
52. Keith, M.; Smith, D.J.; Jenkin, G.R.T.; Holwell, D.A.; Dye, M.D. A review of Te and Se systematics in hydrothermal pyrite from precious metal deposits: Insights into ore-forming processes. *Ore Geol. Rev.* **2018**, *96*, 269–282. [[CrossRef](#)]
53. Škácha, P.; Sejkora, J.; Plášil, J. Selenide mineralization in the Příbram Uranium and base-metal district (Czech Republic). *Minerals* **2017**, *7*, 91. [[CrossRef](#)]
54. Ohmoto, H.; Rye, R.O. Isotopes of sulfur and carbon. In *Geochemistry Hydrothermal Ore Deposits*; Barnes, H.L., Ed.; Wiley and Sons: New York, NY, USA, 1979; pp. 509–567.
55. Ohmoto, H. Systematics of sulfur and carbon isotopes in hydrothermal ore deposit. *Econ. Geol.* **1972**, *67*, 551–578. [[CrossRef](#)]
56. Rajabpour, S.; Behzadi, M.; Jiang, S.Y.; Rasa, I.; Lehmann, B.; Ma, Y. Sulfide chemistry and sulfur isotope characteristics of the Cenozoic volcanic-hosted Kuh-Pang copper deposit, Saveh county, northwestern central Iran. *Ore Geol. Rev.* **2017**, *86*, 563–583. [[CrossRef](#)]
57. Liu, J.J.; Zheng, M.H.; Zhou, D.A.; Liu, J.M.; Zhou, Y.F.; Gu, X.X.; Zhang, B.; Lin, L. The components and evolution of the hydrogen and oxygen isotopes of ore-forming fluids from La'erma gold ore belt. *J. Chang. Univ. Sci. Technol.* **1998**, *28*, 43–49, (In Chinese with English Abstract).
58. Williams-Jones, A.E.; Bowtell, R.J.; Migdisov, A.A. Gold in Solution. *Elements* **2009**, *5*, 281–287. [[CrossRef](#)]
59. Tolstykh, N.; Vymazalová, A.; Tuhý, M.; Shapovalova, M. Conditions of formation of Au–Se–Te mineralization in the Gaching ore occurrence (Maletoyvayam ore field), Kamchatka, Russia. *Mineral. Mag.* **2018**, *82*, 649–674. [[CrossRef](#)]
60. Huston, D.L.; Sie, S.H.; Suter, G.F.; Cooke, D.R.; Both, R.A. Trace elements in sulfide minerals from eastern Australian volcanic-hosted massive sulfide deposits; Part I, Proton microprobe analyses of pyrite, chalcopyrite, and sphalerite, and Part II, Selenium levels in pyrite; comparison with delta ³⁴S values and implications for the source of sulfur in volcanogenic hydrothermal systems. *Econ. Geol.* **1995**, *90*, 1167–1196.
61. Liu, J.J.; Zheng, M.H. Antimonite—No longer just synthetic minerals. *Chin. J.* **1992**, *37*, 1438. (In Chinese)
62. Kolova, E.E.; Savva, N.E.; Zhuravkova, T.V.; Glukhov, A.N.; Palyanova, G.A. Au-Ag-S-Se-Cl-Br mineralization at the Corrida deposit (Russia) and physicochemical conditions of ore formation. *Minerals* **2021**, *11*, 144. [[CrossRef](#)]

Disclaimer/Publisher's Note: The statements, opinions and data contained in all publications are solely those of the individual author(s) and contributor(s) and not of MDPI and/or the editor(s). MDPI and/or the editor(s) disclaim responsibility for any injury to people or property resulting from any ideas, methods, instructions or products referred to in the content.